X-ray diffraction line-profile analysis of hexagonal ϵ-iron-nitride compound layers: composition- and stress-depth profiles

Thomas Gressmann, Andreas Leineweber, Eric Jan Mittemeijer

X-ray diffraction line-profile analysis of hexagonal ε-iron-nitride compound layers: composition- and stress-depth profiles

Journal:	*Philosophical Magazine & Philosophical Magazine Letters*
Manuscript ID:	TPHM-07-Jul-0199.R1
Journal Selection:	Philosophical Magazine
Date Submitted by the Author:	24-Oct-2007
Complete List of Authors:	Gressmann, Thomas; Max Planck Institute for Metals Research Leineweber, Andreas; Max Planck Institute for Metals Research Mittemeijer, Eric Jan; Max Planck Institute for Metals Research, Prof. Dr Ir. E.J. Mittemeijer
Keywords:	metallic materials, microstructural characterization, nitrides, stress analysis, X-ray diffraction
Keywords (user supplied):	line-profile analysis, grain interaction, anisotropic thermal expansion

X-ray diffraction line-profile analysis of hexagonal ε-iron-nitride compound layers: composition- and stress-depth profiles

T. GRESSMANN, A. LEINEWEBER*, E. J. MITTEMEIJER

Max Planck Institute for Metals Research, Heisenbergstraße 3, D-70569 Stuttgart, Germany

*corresponding author

Authors:

Thomas Gressmann
Tel.: +49 711 689 3369
E-mail: t.gressmann@mf.mpg.de;

Dr. Andreas Leineweber
Tel.: +49 711 689 3365
E-mail: a.leineweber@mf.mpg.de;

Prof. Dr. Ir. Eric Jan Mittemeijer
Tel.: +49 711 689 3311
E-mail: e.j.mittemeijer@mf.mpg.de;

Max Planck Institute for Metals Research, Heisenbergstrasse 3, D-70569 Stuttgart, Germany

Fax: +49 711 689 3312

Abstract

Two hexagonal ε-Fe_3N_{1+x} layers grown on α-Fe substrates by nitriding in NH_3/H_2 gas atmospheres were investigated by high-resolution X-ray powder diffraction using synchrotron radiation employing systematic tilting of the diffraction vector with respect to the specimen surface. The obtained complicatedly shaped diffraction profiles, considering all recorded reflections simultaneously, were analysed using a model incorporating *hkl*-dependent (anisotropic) and tilt-angle (ψ) dependent diffraction-line broadening and diffraction-line shifting. The diffraction-line broadening is mainly ascribed to the nitrogen concentration-depth profile within the layers causing depth-dependent strain-free lattice parameters, whereas the line shifts are predominantly caused by the stress-depth profile originating from the concentration-dependence of the coefficients of thermal expansion of the ε phase, with stress parallel to the surface which is of tensile nature at the surface and of compressive nature at the ε/γ´ interface. This stress gradient additionally leads to a ψ-dependence of the line broadening. Fitting of the microstructure and diffraction model led to determination of microstructure parameters, which can be related to the different sets of treatment conditions applied for the ε-iron-nitride layer growth.

Keywords: metallic materials, stress analysis, X-ray diffraction, nitrides, microstructural characterization, line-profile analysis, grain interaction, anisotropic thermal expansion

1 Introduction

In the field of materials science there is a great demand for methods for depth-dependent characterisation of the microstructure of polycrystalline thin films and surface layers, especially recognising that in many specimens/workpieces the properties change with depth. Depth profiling by determination of depth-dependent (micro-)structural features (e.g. lattice parameters – associated with composition, macrostresses, microstresses, crystallite size), is often realised in a destructive manner either by cutting a piece out of the specimen/workpiece of interest and investigation of the thus produced cross section (e.g. by electron probe microanalysis (EPMA)), or by successive removal of sublayers of material from the surface by methods like polishing and analysis of the occurring surface or near surface volume (e.g. by means of X-ray diffraction (XRD)) [1]. These types of depth profiling are destructive and, moreover, upon removal of material from the surface the characteristics of the investigated material may change, e.g. a redistribution of stress in the remaining material occurs because of the requirement of mechanical equilibrium and also stress may be induced by the removal of material. Hence, a non-destructive method is desired. The method developed and applied in this work is based on non-destructive high-resolution X-ray powder-diffraction analysis: The positions and full shapes of diffraction-line profiles recorded under variation of the orientation of the diffraction vector with respect to the surface are interpreted in terms of an absorption-weighted superposition of the diffraction effects in the detected signal arising from different depths and as influenced by changes in composition and stress.

[Insert Fig. 1 about here]

The system iron-nitrogen is not only scientifically of great interest in metallurgy but also plays an important role in technology [2, 3]: in particular iron-nitride phases as surface layers on iron or steel workpieces are of great importance, since they can improve the corrosion resistance and the tribological properties of the surface region [4, 5]. Iron-nitride phases are typically generated by nitriding iron or steel in NH_3/H_2 gas mixtures at temperatures between 773 K and 863 K. During the nitriding process the α-iron substrate becomes enriched with nitrogen and, if the chemical potential of nitrogen in the applied gas mixture is sufficiently high, a compound layer forms composed of an outer surface-adjacent ε-Fe_3N_{1+x} sublayer (for the ε phase also formulas like Fe_2N_{1-z} and FeN_y with $y = (1 + x)/3$ are used in literature) and an inner γ′-Fe_4N sublayer adjacent to the α-iron substrate (Fig. 1)[1]. Both, the ε and the γ′ phase contain a close-packed stacking of the iron atoms, with *hcp* for ε and *fcc* for γ′, in which the nitrogen atoms occupy octahedral interstitial sites in a more or less long-range ordered fashion [6-10]. Especially the ε phase is of great interest, since its homogeneity range is quite large, e.g. at 823 K from about 24 at.% N to about 33 at.% N [11] (Fig. 2). These concentration variations are associated with considerable variations of the lattice parameters *a* and *c*. It is well known that within the ε layer a concentration gradient builds up during the nitriding process due to the inward diffusion of nitrogen from the gas atmosphere to the bulk [12], with *higher* nitrogen contents at the surface of the specimen and with *lower* nitrogen contents at the ε/γ′ interface, implying a strong depth dependence of the lattice parameters. Various dependencies of the lattice parameters on the composition of the ε phase have been reported [7, 13-18]. The data from the different sources vary considerably. Furthermore, it was shown recently that the lattice parameters depend not only on the nitrogen content but also to a significant extent on the degree of nitrogen ordering induced by the type of cooling procedure employed after nitriding or heat treatment [18].

[1] For nitriding steels, composed of many different alloying elements, often no clear distinction between the sublayers is possible.

[Insert Fig. 2 about here]

Additional to the concentration gradient, a macrostress-depth profile will likely build up within the ε layer. Residual macrostresses can arise when different parts/phases of a cohesive specimen tend to assume different volumes. Thus concentration-depth profiles and misfit between layer and substrate can induce a state of stress in a surface layer. Detailed information on and fundamental understanding of the macrostresses present in ε layers lacks. Until now a few publications provide data on macrostresses in ε layers, unfortunately mostly dealing with steels nitrided by commercial treatments without giving much detail [19-21], which hinders a straightforward interpretation of the obtained results. The work by Somers and Mittemeijer, 1992 [21] can be regarded as the most comprehensive one, dealing also with pure nitride compound layers on pure α-iron. In all previous works only diffraction-line (peak) positions were analysed. The present work deals with non-destructive *high-resolution X-ray powder-diffraction* investigation of hexagonal ε-Fe_3N_{1+x} layers grown on top of α-iron substrates by gas nitriding, thereby allowing detailed (shape) analysis of the full line profiles. A model for the microstructure has been developed which, upon fitting to the diffraction data, leads to determination of the depth profiles of the macrostrain-free lattice parameters and the macrostress, simultaneously considering several *hkl*-reflections recorded at different specimen tilt angles ψ.

2 Experimental

2.1 Specimen preparation

Iron rods were prepared from pure iron (Alfa Aesar, 99.98 wt.%) in an inductive furnace under argon atmosphere (99.999 vol.%). The casts were cold-rolled to plates of about 1 mm thickness. These sheets were cut into rectangular pieces (20 mm × 25 mm) and annealed for 2 h at 973 K under flowing hydrogen to obtain a recrystallised grain structure. Before nitriding the specimens

were ground, polished (last step: 1 µm diamond paste) and cleaned in ethanol in an ultrasonic bath.

For nitriding the specimens were suspended by quartz fibres in the middle of a vertical quartz-tube furnace equipped with a water container for quenching. The nitriding experiments were performed in NH_3 (99.999 vol.%) / H_2 (99.999 vol.%) gas mixtures at 823 K. The fluxes of both gases were adjusted using mass-flow controllers and amounted together to 500 ml/min (referring to the gas volume at room temperature), which corresponds to a linear gas velocity of 13.5 mm/s through the quartz retort (diameter 28 mm), which is sufficiently high in order to minimise the effect of ammonia decomposition. After the thermochemical heat treatments the quartz fibres were cut within the furnace and thus the specimens were quenched by dropping into water at room temperature flushed with N_2. The treatment parameters of the two analysed specimens, further denoted as specimen *A* and *B*, have been listed in Table 1.

[Insert Table 1 about here]

Specimen *B* was subdivided into two parts of equal size. One part was subjected to a subsequent heat treatment in order to remove by homogenisation the concentration gradient within the ε layer [22]. To this end this part of the specimen was encapsulated into a quartz tube under residual Ar pressure (300 mbar). The annealing occurred in a salt bath at 673 K for 1 day. After the heat treatment the specimen was quickly removed from the salt bath and quenched by throwing the tube (without crushing) into cold water. During the homogenisation process the nitrogen concentration of the ε phase in the specimens adjusts to the value pertaining to equilibrium of ε with γ′ according to the phase diagram (Fig. 2) [23].

2.2 Metallography

For light-optical microscopy a small part of each specimen was cut and covered with a protective nickel layer by electrodeposition using a Watts bath [24, 25] at 333 K in order to avoid curvature and damaging close to the surface of the specimen during subsequent metallographic handling. Next, the pieces were embedded (Polyfast, Buehler GmbH), ground, polished (last step: 1 µm diamond paste) and finally etched using 1 vol.% Nital containing 0.1 vol.% HCl [26]. Light-optical microscopy was performed with a Leica DMRM microscope. For each specimen several cross-sectional micrographs were taken close to both faces of the specimens. The layer thicknesses were determined from these micrographs: the measured area of the layer was divided by the measured lateral length of the layer, yielding the layer thickness (Table 1). The values of several micrographs were arithmetically averaged [22]. By this method the effect of the slight interface roughness is averaged out.

2.3 TEM and EBSD

High-resolution transmission electron microscopy (TEM) and electron back-scattering diffraction (EBSD) were performed to investigate the orientation relationship between the ε and the γ′ layer. TEM on cross-sections at the ε/γ′ interface region was carried out using a JEOL JEM-4000FX (400 kV) transmission electron microscope. The preparation procedure of the TEM foils is described elsewhere [27, 28]. For EBSD measurements, performed on cross-sections, the specimens were embedded, ground and polished (last step: colloidal silica suspension OPS, Struers GmbH, for several hours). EBSD was carried out using a Zeiss scanning electron microscope equipped with an EBSD system (TSL, EDAX, Inc.). Indexing and analysis of the recorded Kikuchi patterns was done using the software OIM 3.5.

2.4 X-ray diffractometry

High-resolution X-ray powder-diffraction analysis was carried out at the synchrotron beamline B2, HASYLAB, Hamburg. The station was equipped with a Eulerian cradle and used in direct

beam configuration [29]. The wavelength was adjusted to 0.80017 Å, in order to achieve a relatively low X-ray absorption (cf. section 3.2). The cross-section of the beam was set to 5 mm × 1 mm, in order to ensure that the whole beam hits the surface of the specimen and that as much surface area as possible is illuminated for all applied specimen orientations. The diffracted beam passed a Ge(111) analyser crystal before being detected by a NaI scintillation counter. During the measurements the samples were rotated around the surface normal in order to achieve better crystallite statistics (rotational symmetry of the state of stress within the plane of the specimen was assumed: $\sigma_{//} \equiv \sigma_{11} = \sigma_{22}$). For stress measurements the diffractometer was used in χ mode[2] [30, 31] in symmetrical diffraction geometry and the applied specimen tilt angles ψ ranged from 0° to 60°. The step size in 2θ was varied *hkl* dependently between 0.002° and 0.008°. The following 9 reflections pertaining to the ε phase were recorded for both specimens in the 'as-nitrided' state by measuring over sufficiently large 2θ subranges: 110, 002, 111, 112, 300, 113, 302, 223 and 304. These *hkl* refer to the hexagonal superstructure with $a = 3^{1/2}a_{hcp}$ and $c = c_{hcp}$; the index *hcp* refers to the unit cell of the *hcp* type arrangement of the iron atoms. Weak superstructure reflections due to nitrogen ordering were not considered in the measurements. Additionally, selected reflections of SRM660a LaB_6 (NIST, USA) were measured as a standard to determine the instrumental resolution, as well as reflections were recorded from the annealed, homogenised part of specimen *B* for determining the remaining diffraction-line broadening due to thermal misfit induced microstresses (see section 3.3) of homogenised ε-Fe_3N_{1+x} layers.

[2] χ is the angle of rotation of the sample around the axis defined by the intersection of the diffraction plane and sample surface, i.e. perpendicular to the $\theta/2\theta$ plane; χ coincides in χ mode with the angle ψ.

3 Theoretical considerations

3.1 Model for the microstructure of ε layers

The microstructure of *hcp* ε-Fe_3N_{1+x} layers can be modelled recognising that at each depth below the surface a plane of constant lattice parameters and a constant state of stress is present and adopting an ideally flat ε/γ′ interface.

3.1.1 Lattice-parameter depth profile

Compositional variations within a single, crystalline phase are generally associated with lattice-spacing variations. According to the applied nitriding conditions relatively large depth(z)-dependent nitrogen-concentration variations are expected to be present within the ε layers (cf. Table 1), implying depth-dependent hexagonal lattice parameters $a(z)$ and $c(z)$. Then, for each hkl, the corresponding depth-dependent lattice spacing $d_{hkl}(z)$ can be calculated according to:

$$d_{hkl}^{-2}(z) = \tfrac{4}{3}a^{-2}(z)(h^2 + k^2 + hk) + c^{-2}(z)l^2 . \qquad (1)$$

Composition dependencies of a and c are known, as e.g. reported in Refs. [17, 18]. Also a significant degree-of-order (in the nitrogen superstructure) dependence of a and c has been reported [18]. In order to allow maximum flexibility in the model, the strain-free lattice parameters a and c are allowed to vary independently (see section 4.3).

[Insert Fig. 3 about here]

[Insert Fig. 4 about here]

The ε layers of thickness Z were considered to be composed of a sufficient number of n sublayers ($n = 5$ for sample A and $n = 8$ for sample B) of equal thickness, $\delta z = Z/n$ [3]. Thus, the sublayer/sublayer interfaces, further denoted as grid points (GP in Figs. 3 and 4), are located at depth $z_j = j\delta z$, with $j = 0, 1, \ldots, n$, below the specimen surface (Fig. 3). The lattice parameters are

[3] δX denotes the *change* of a variable/function X over a sublayer j ($\delta X(j)$), e.g. δz, $\delta d_{hkl}(j)$ or $\delta d_{hkl}^{-2}(j)$ (see Figs. 3 and 4) or over the whole ε layer (δX with superscript 'total').

assumed to decrease monotonously with increasing distance to the surface and at the grid points have values $a(j)$ and $c(j)$. The j^{th} sublayer occurs between the grid points $j-1$ and j. Within a sublayer the lattice parameters a and c are linearly interpolated with respect to the values of the corresponding grid points. This leads to a partitioning of the functions $a(z)$ and $c(z)$ over the whole layer. The d spacing at the grid points and the partitioned function $d_{hkl,0}(z)$ (see Fig. 3) can then be calculated straightforwardly from the corresponding values from the lattice parameters a and c using Eq. (1)[4].

3.1.2 Stress-depth profile

The compound layers are produced by gas nitriding of polycrystalline substrates and thus the ε layers should exhibit a rotationally symmetric biaxial state of stress parallel to the surface of the specimen, i.e. $\sigma_{//} \equiv \sigma_{11} = \sigma_{22}$ (similar to the observations made in Ref. [32] on γ′ layers). Effects originating from the edges of the specimens can be ignored for the irradiated area in the experiment. The stress is assumed to change linearly with depth within the layers so that at the grid points j the stress corresponds to

$$\sigma_{//}(j) = \sigma_{//}(j=0) + \frac{j\delta z}{Z}\delta\sigma_{//}^{\text{total}}, \qquad (2)$$

where $\sigma_{//}(j=0)$ denotes the stress value at the surface of the specimen and $\delta\sigma_{//}^{\text{total}}$ represents the total change in stress over the whole layer. Linearity of the stress gradient is assumed in order to keep the model as simple as possible, without loosing physically relevant information. Such a macrostress-depth profile, $\sigma_{//}(z)$, leads to ψ- and depth-dependent mechanical strains and lattice spacings $d_{hkl,\psi}(z)$, where ψ is the specimen-tilt angle (angle between surface normal and diffraction vector; see also footnote 2).

[4] Small changes $\delta a(j) = a(j) - a(j-1)$ and $\delta c(j) = c(j) - c(j-1)$ with respect to $a(j-1)$ and $c(j-1)$, as well as linear dependence on depth of a and c within the sublayers leads to an, also, practical linear dependence on depth of $d_{hkl}^{-2}(z)$ and $d_{hkl}(z)$ within each sublayer.

It can be shown that $d_{hkl,\psi}$ depends linearly on $\sin^2\psi$ (e.g. see Ref. [30]):

$$d_{hkl,\psi}(j) = \left[\left(2S_1^{hkl} + \tfrac{1}{2}S_2^{hkl}\sin^2\psi\right)\sigma_{//}(j) + 1\right] d_{hkl,0}(j) \qquad (3a)$$

where $d_{hkl,0}$ denotes the strain-free lattice spacing and S_1^{hkl} and $\frac{1}{2}S_2^{hkl}$ are the so-called X-ray elastic constants (XECs). The calculated single-crystal elastic constants (SECs) of stoichiometric ε-Fe_3N indicate a very small intrinsic elastic anisotropy (see Appendix) which will be neglected here[5]. In that case the X-ray elastic constants (XECs) are independent of *hkl* and Eq. (3a) can be written as

$$d_{hkl,\psi}(j) = \left[\left(-2\frac{\nu}{E} + \frac{1+\nu}{E}\sin^2\psi\right)\sigma_{//}(j) + 1\right] d_{hkl,0}(j) \qquad (3b)$$

with E as Young's modulus and ν as Poisson ratio.

3.2 Diffraction effects of the microstructure model

The intrinsic diffraction-line profiles of the ε layers can in principle (see below) be calculated on the basis of the microstructure model described in section 3.1. This leads to a line profile, denoted here as f'', which has to be convoluted with line-profile contributions g and f' as described in section 3.3, to obtain the overall diffraction pattern that can be considered as a simulation of the experimentally recorded one.

For calculation of the intrinsic diffraction-line profile f'' it is assumed that each – infinitesimally thin – slice of the ε layer with a given lattice spacing $d_{hkl,\psi}$ diffracts independently and produces its own diffraction subline profile. Coherency effects (of diffraction) are not considered, i.e. the integrated (diffracted) intensities of the slices are additive.

The layer consists mainly of columnar grains; viz. ε-ε grain boundaries are generally perpendicular to the surface of the specimen (see section 4.1) and thus a possible texture can be

[5] Application of calculated *hkl*-dependent XECs (used as S_1^{hkl} and $\frac{1}{2}S_2^{hkl}$ in Eq. (3a)) recognising the slight anisotropy of the SECs and calculated using different methods for grain interaction (e.g. Refs. [33, 34]) did not lead to an improvement of the fitting results described in section 4.3.

taken as depth independent. Finally, it is assumed that the scattering power of the iron nitride does not vary with depth recognising the modest changes in nitrogen content and correspondingly modest changes of unit-cell volume and the structure factor.

The diffraction angle at which the diffraction contribution of a reflection *hkl*, at a given ψ, pertaining to a slice at grid point *j* occurs is given by

$$2\theta_{hkl,\psi}(j) = 2\theta_{hkl,\psi}(j=0) + \sum_{j'=1}^{j} \delta 2\theta_{hkl,\psi}(j'), \qquad (4)$$

where the reflection shift $\delta 2\theta_{hkl,\psi}(j) = 2\theta_{hkl,\psi}(j) - 2\theta_{hkl,\psi}(j-1)$ over the sublayer *j* can be calculated by using Bragg's law: $\delta 2\theta_{hkl,\psi}(j) = -2\dfrac{\delta d_{hkl,\psi}(j)}{d_{hkl,\psi}(j)} \tan\theta_{hkl,\psi}(j)$. Because $-2\,\delta d_{hkl,\psi}(j)/d_{hkl,\psi}(j) = \delta d^{-2}_{hkl,\psi}(j)/d^{-2}_{hkl,\psi}(j) \approx \delta d^{-2}_{hkl,\psi}(j)/d^{-2}_{hkl,\psi}(j=0)$ and $\tan\theta_{hkl,\psi}(j) \approx \tan\theta_{hkl,\psi}(j=0)$ it is finally obtained:

$$\delta 2\theta_{hkl,\psi}(j) = \frac{\delta d^{-2}_{hkl,\psi}(j)}{d^{-2}_{hkl,\psi}(j=0)} \times \tan\theta_{hkl,\psi}(j=0). \qquad (5)$$

The total line width $\delta 2\theta^{\text{total}}_{hkl,\psi}$ is given by the sum of the line-width contributions of the sublayers, $\sum_{j=1}^{n} \delta 2\theta_{hkl,\psi}(j)$ (Fig. 4).

Neglecting at first the effect of X-ray absorption, (i) the integrated intensity originating from each sublayer is the same, since the amount of diffracting material is the same for each sublayer, and (ii) the intensity diffracted by the sublayer is distributed homogeneously over the width $\delta 2\theta_{hkl,\psi}(j)$, since the lattice-spacing gradient is virtually constant within the sublayer due to the linear variation of *a* and *c* and of the strain (see section 3.1) and the relation between *d* and 2θ is approximately linear for small ranges in *d* and 2θ (cf. Bragg's law). Since the grid points, for a given *hkl* and ψ, are not equidistantly distributed on the 2θ scale, the same amount of integrated intensity (again ignoring the absorption of X-rays) is distributed over different diffraction-angle

ranges $\delta 2\theta_{hkl,\psi}(j)$ (Fig. 4): The smaller the lattice-parameter variation over a sublayer j is, the smaller $\delta 2\theta_{hkl,\psi}(j)$ and the higher the intensity of the sublayer are in the composite reflection *hkl*. The relative intensity (height) originating from sublayer j is given by the factor $\left[\delta d_{hkl,\psi}^{-2}(j)\right]^{-1}$ (cf. Eq. (5)).

The X-rays are absorbed along their way through the ε layer. Therefore, the diffracted intensity originating from a depth z below the surface gets attenuated according to

$$I(z) = I_S \exp(-\mu(\lambda) k_\psi z), \qquad (6)$$

where $I(z)$ denotes the observed intensity pertaining to (the slice at) depth z below the surface and I_S represents the intensity at the state of reference (slice at the surface of the specimen). $\mu(\lambda)$ is the (effective) linear absorption coefficient of the traversed material pertaining to the applied wavelength λ and k_ψ is a diffraction-geometry dependent factor, which reads for the applied diffraction geometry $k_\psi = 2/(\sin\theta\cos\psi)$. The value of $\mu(\lambda)$ can be calculated as a composition-weighted sum of the linear absorption coefficients of Fe and N for Fe_3N at $\lambda = 0.80017$ Å; i.e. $\mu_{Fe_3N}(0.8Å) = 0.035\ \mu m^{-1}$ [35]. It is assumed that for the modest compositional variations of the ε layers $\mu(\lambda)$ can be taken as constant.

3.3 Data evaluation method

The total line profiles h of the ε layers were calculated as the convolution of three different contributions:

$$h = g \otimes f' \otimes f'' \qquad (7)$$

where g represents the instrumental broadening contribution, where f' denotes a physical *hkl*-dependent structural broadening contribution typical for even homogeneous ε-iron nitrides [36] (see below), and where f'' denotes the intrinsic, structural broadening contribution according to the model for the microstructure described in sections 3.1-3.2.

The contributions g and f' for the different measured reflections were described by split pseudo-Voigt (spV) functions similar as reported by Liapina et *al*., 2006 [36], i.e. by

$$g_{hkl}(x), f'_{hkl}(x) = \frac{(1-\eta_{hkl}^{g,f'})}{B_{hkl}^{g,f'}}\sqrt{\frac{\ln 16}{\pi}}\exp\left(-\frac{\ln 16 \times x^2}{\left(B_{hkl}^{g,f'}\right)^2\left(1 \pm As_{hkl}^{g,f'}\right)^2}\right) + \frac{2\eta_{hkl}^{g,f'}}{\pi B_{hkl}^{g,f'}\left(4x^2 \Big/ \left(\left(B_{hkl}^{g,f'}\right)^2\left(1 \pm As_{hkl}^{g,f'}\right)^2\right)+1\right)} \quad (8)$$

with $x = 2\theta_{hkl} - 2\theta_{0,hkl}$ ($2\theta_{0,hkl}$: fitted peak maximum) and $B_{hkl}^{g,f'}$ denotes the full width at half maximum (FWHM). $As_{hkl}^{g,f'}$ and $\eta_{hkl}^{g,f'}$ are peak shape parameters, where $\eta_{hkl}^{g,f'}$ is a mixing parameter leading for $\eta_{hkl}^{g,f'} = 0$ to Gaussian broadening and for $\eta_{hkl}^{g,f'} = 1$ to Lorentzian broadening, and $\pm As_{hkl}^{g,f'}$ quantifies the peak asymmetry with '–' for $x > 0$ and '+' for $x < 0$. The instrumental broadening g was determined from the reflections measured on the LaB_6 standard powder at $\psi = 0°$ (measurements at $\psi = 30°$ and $\psi = 60°$ were also conducted, indicating no significant ψ dependence of the peak shapes): Diffraction-angle dependent polynomials for B^g, As^g and η^g were determined on the basis of B_{hkl}^g, As_{hkl}^g and η_{hkl}^g, which allows to determine the instrumental broadening at an arbitrary diffraction angle, as required for analysis of the diffraction data from the ε-iron-nitride layers.

The contribution f' was determined from the homogenised ε layer. For each recorded reflection *hkl* of this layer the instrumental-broadening function g (pertaining to the corresponding diffraction angle, see above) was convoluted with a split pseudo-Voigt function to describe f'_{hkl} according to Eq. (8). Then by fitting $g \otimes f'$ to the measured reflection of the homogenised ε layer values for $B_{hkl}^{f'}$, $As_{hkl}^{f'}$ and $\eta_{hkl}^{f'}$ were obtained. It was found that the *hkl* dependence of $B_{hkl}^{f'}$ and $As_{hkl}^{f'}$ resembles that of the 'residual' diffraction-line broadening observed previously for homogenised ε-iron-nitride powders of composition similar to the present homogenised ε layer [36].

The ε reflections of the homogenised part of specimen *B* (data not shown) are much narrower than the ε reflections recorded from the layers in the 'as-nitrided' state, but are significantly broader than those of the standard LaB_6 at similar 2θ values. The broadening of the profile f' is of microstrain-like character (the line width of a series of higher-order reflections increases with $\tan\theta_{hkl}$), and is strikingly asymmetric and anisotropic: reflections at and close to $\varphi_{hkl} = 0°$ (φ_{hkl} is the angle of the diffraction vector with the [001] direction of the diffracting crystallites; e.g. $\varphi_{hkl} = 0°$ for 00*l* reflections) show low-angle tails, whereas reflections at and close to $\varphi_{hkl} = 90°$ (e.g. 110, 300) show high-angle tails. The microstrain in the direction of the diffraction vector has maximum values at $\varphi_{hkl} = 0°$ and $\varphi_{hkl} = 90°$. A minimum of microstrain occurs at $\varphi_{hkl} \approx 45°$. The *hkl*-dependent, anisotropic and asymmetric line-broadening contribution f' may be understood to be due to minor compositional variations within the homogenised ε layer (unlikely) and/or to be caused by microstresses invoked during cooling by the anisotropy of the thermal shrinkage (likely). The absolute $B_{hkl}^{f'}$ values are significantly larger in the present case than in the study on homogenised ε-iron-nitride powders [36]. This difference may be ascribed to a different microstructure and different thermal treatment leading to anisotropic thermal microstrain different in the annealed, homogenised *layer* as compared to the annealed *powder*. In the same sense it can be understood that the refinements described in the following indicate that the *extent* of f' in the *not-homogenised ε layer* is somewhat smaller than in the *homogenised ε layer*, e.g. due to difference in the annealing temperature of the homogenised ε layer and the nitriding temperature of the not-homogenised ε layers. It was found that adopting values of $\frac{2}{3} B_{hkl}^{f'}$, with $B_{hkl}^{f'}$ as determined from the homogenised ε layer, led to consistent interpretation of all diffraction data recorded from the not-homogenised ε layers.

Given the contribution $g \otimes f'$ for each line profile, the total line profile *h* can be calculated applying Eq. (7) where f'' is calculated according to the microstructural model described in sections 3.1 and 3.2. The thus obtained profile *h* can be fitted to the measured data by

determination of optimal values of the fit parameters incorporated in the microstructural model for f''. These fit parameters are: the strain-free lattice parameters at the grid points j, $a(j)$ and $c(j)$, the stress value at the surface of the specimen, $\sigma_{//}(j = 0)$, the total change in stress over the whole layer, $\delta\sigma_{//}^{\text{total}}$. Such fitting was performed for all recorded reflections and all tilt angles ψ *simultaneously*.

Refinement of $a(j)$ and $c(j)$ without any constraints leads to strong correlations of the lattice parameters of neighbouring grid points and to partially physically unreasonable a and c depth profiles. The correlations can be reduced, and physically realistic, 'smoother' $a(j)$ and $c(j)$ depth profiles can be obtained, by application of so-called penalty functions (*PF*s). Such *PF*s serve as contribution to the overall χ^2_{pen} (*penalized least squares*) used in the least-squares refinement process, additional to the usual least-squares χ^2 determined by the difference between the observed and the calculated profiles [37, 38]:

$$\chi^2_{pen} = \chi^2 + (K \cdot PF)^2 , \qquad (9)$$

where K denotes a penalty-weighting factor [39].

The *PF* applied in this work is the sum of the squared differences between $\delta a(j)$ and $\delta a(j + 1)$ and $\delta c(j)$ and $\delta c(j + 1)$ for each value of j:

$$PF = \sum_{j=1}^{n-1} (\delta a(j) - \delta a(j+1))^2 + \sum_{j=1}^{n-1} (\delta c(j) - \delta c(j+1))^2 . \qquad (10)$$

The *PF* is minimal ($PF = 0$) for a linear evolution of $a(j)$ and $c(j)$ over the whole layer thickness, i.e. $\delta a(j)$ and $\delta c(j)$ are constant for all sublayers j.

A compromise for the weight K of the penalty-function contribution to the overall χ^2 has to be found in order to obtain reasonable results: In the case of a too large weight, physical features in $a(z)$ and $c(z)$ may be suppressed ('oversmoothing') and in the case of a too small weight, $a(z)$ and $c(z)$ can vary too unconstrainedly [40]. Consistent and realistic results were obtained by

allowing the penalty function to increase the χ^2 value by not more than about 20 % with respect to the unconstrained refinement.

The least-squares fitting procedures as described above were executed using the programming language available in the launch mode of the TOPAS software [39]. For determination of the optimal values for the fit parameters pertaining to f'' (see above), so-called 'Pawley fits' were performed, i.e. allowing free refinement of the total integrated reflection intensity of each refection *hkl* and at each ψ separately.

4 Results and discussion

4.1 Microstructure of the ε layers, as determined by optical microscopy, TEM and EBSD

Optical microscopy (Fig. 1) and EBSD (Fig. 5) revealed that the ε layers of both samples consist predominantly of columnar grains, i.e. the ε grains extend from the surface of the specimen to the ε/γ′ interface with grain boundaries mostly parallel to the specimen surface normal. The ε/γ′ interface shows only slight roughness. Analysis of the EBSD data indicates that there is no distinct orientation relationship between γ′ and ε; the ε grains grow largely randomly oriented on top of γ′. EBSD and also the ψ dependence of the diffracted intensities of the XRD data (not shown in detail here) indicate that the ε layers investigated exhibit an only weak 001 fibre texture, which is probably a growth texture, because of the absence (see above) of a distinct orientation relationship between the ε and the γ′ grains (also the γ′ layer shows no preferred orientation, cf. Ref. [32]).

High-resolution cross-sectional TEM studies at the location of the ε/γ′ interface confirm that no specific orientation relationship, as reported in Refs. [28, 41-45], occurs between ε and γ′. TEM also showed that neither in the ε layer (Fig. 6) nor in the γ′ layer at/near the interface stacking faults are present; stacking faults could lead to special line-shift and line-broadening effects in the powder-diffraction patterns.

[Insert Fig. 5 about here]

[Insert Fig. 6 about here]

4.2 Qualitative description of the diffraction-line profile and preliminary analysis

(i) Line position and line width

The diffraction patterns recorded for samples *A* and *B* (Fig. 7) revealed a characteristic, anisotropic variation of the line positions and line broadening, both as function of the angle of the diffraction vector with the sample normal, corresponding to the tilt angle ψ (i.e. with respect to the *specimen frame of reference*), as well as function of the angle of the diffraction vector with the [001] direction of the diffracting crystallites, φ_{hkl} (i.e. with respect to the *crystal frame of reference*; e.g. $\varphi_{hkl} = 0°$ for 00*l* reflections and $\varphi_{hkl} = 90°$ for *hk*0 reflections).

For both samples, reflections with the diffraction vector direction parallel to the [001] direction ($\varphi_{hkl} = 0°$), exhibit much smaller line-broadening widths, $\delta 2\theta^{\text{total}}_{hkl,\psi}$, than reflections with the diffraction vector perpendicular to the [001] direction, e.g. 110, 300 ($\varphi_{hkl} = 90°$), which are generally the broadest reflections. In general *f*′′ is much broader than the instrumental broadening *g* and the line-broadening contribution *f*′ originating from a homogenised ε layer.

Upon comparing the diffraction patterns of samples *A* and *B* recorded at a given ψ and for a given reflection *hkl*, the high-angle edge of the reflections, originating from the region at the ε/γ′ interface, appears for both specimens almost at the same 2θ position, whereas this is not the case for the low-angle edges of the reflections, pertaining to the surface adjacent region: for specimen *A* the low-angle side is located at higher 2θ values than for specimen *B*. Furthermore, with increasing ψ for all ε reflections of both specimens the low-angle edge of the reflection shifts towards lower 2θ values, whereas the shape change at the high-angle edge (see below) does not allow a similar conclusion. The ψ-dependent shift of in particular the low-angle edge leads to a ψ

dependence of the line broadening: reflections recorded at higher ψ angles are generally broader than reflections recorded at lower ψ angles.

The φ_{hkl}-dependent (i.e. with respect to the crystal frame of reference) anisotropic line broadening at a given ψ can be understood by lattice-parameter variations due to compositional variations [46] associated here with the presence of the nitrogen-concentration gradient within the ε layer. Since variation of the nitrogen content leads to larger relative changes of the lattice parameter a than of the lattice parameter c [17, 18], reflections with φ_{hkl} close to 0° (see above) should exhibit smaller $\delta 2\theta^{\text{total}}_{hkl,\psi}$ values than reflections with φ_{hkl} close to 90°, in agreement with the observations described above.

The more pronounced line broadening (valid for all reflections) observed for specimen *B*, in comparison with specimen *A*, can be explained as follows: Specimen *B* was prepared applying a higher nitriding potential than applied for specimen *A* (cf. Table 1), leading, at the surface of specimen *B*, to a higher nitrogen content and consequently to larger lattice spacings at the surface than for specimen *A*. At the ε/γ′ interface the nitrogen content and thus the lattice spacings of specimens *A* and *B* are expected to be similar, supposing local equilibrium of ε and γ′ at the nitriding temperature. Thus the total change of lattice spacing over the ε layer, and thereby the corresponding total line broadening, is expected to be larger for specimen *B* than for specimen *A*, as observed.

The increase of the line broadening, characterised by the line-width parameter $\delta 2\theta^{\text{total}}_{hkl,\psi}$, with increasing ψ (i.e. with respect to the specimen frame of reference), observed for all reflections of both specimens, can be related to the stress-depth profile within the ε layers (cf. section 4.3.2): With increasing ψ the low-angle edge of a reflection is shifted to lower 2θ angles due to tensile stress at the surface, whereas the high-angle edge of the same reflection will remain at the same position 2θ, if no stress is present in ε at the ε/γ′ interface, or shift to higher angles 2θ,

if compressive stress prevails in ε at the ε/γ′ interface. Then the total width, $\delta 2\theta_{hkl,\psi}^{\text{total}}$, increases with increasing ψ, as observed.

(ii) Line shape

Alongside with the line-width changes due to variations of the diffraction-vector direction with respect to the crystal frame of reference (characterised by the angle φ_{hkl}) and with respect to the specimen frame of reference (characterised by the angle ψ), characteristic changes of the line shape occur. Reflections of specimen *A* with φ_{hkl} close to 90° exhibit a more or less rectangular shape, whereas similar reflections of specimen *B* show characteristic high-angle tails. In general the high-angle part of these reflections, with φ_{hkl} close to 90°, gets attenuated with increasing ψ with respect to the low-angle part (see Fig. 7). Reflections with low φ_{hkl} values are relatively narrow and show no pronounced asymmetry. For some of these reflections (e.g. 002) even slight low-angle tails occur; such tails are also present in the contribution *f′* pertaining to homogenised ε, emphasising the need of including contribution *f′* in the line-broadening analysis (see section 3.3). Note that the (apparent) shape of the ε-002 reflection of specimen *A* is affected by the 111 reflection of the γ′-Fe_4N layer underneath this (thin) ε layer. The γ′-111 reflection of specimen *A* appears at strongly ψ-dependent peak positions, due to a relatively large compressive stress within the γ′ layer (see Ref. [32]). This 111 reflection of the γ′ phase is not visible for specimen *B* because of the larger ε-layer thickness of that specimen.

The ψ-dependent change in peak shape can be ascribed to the absorption of the X-rays. The rectangular shape of almost all reflections of the ε layer of specimen *A* (with exception of the narrow reflections with small φ_{hkl} values) measured at $\psi = 0°$ is due to the low absorption of the X-rays by this relatively thin ε layer: a range of more or less equally probable lattice spacings, as pertaining to an almost linear lattice-spacing depth profile, will, in case of negligible absorption of the X-rays, generate such peak shapes. With increasing ψ, and in particular for the larger ε-layer thickness of specimen *B*, the incident and diffracted X-rays in the bottom region of the ε layer are

significantly absorbed due to, the, for higher ψ angles and larger ε-layer thickness, longer paths the X-rays have to travel through the solid (see also section 3.2). Since with increasing distance to the surface the lattice spacings get smaller, the X-ray attenuation affects, in particular, the high-angle sides of the reflections causing the characteristic high-angle tails, especially pronouncedly visible for specimen *B* (Fig. 7(b)). This effect is less distinctly visible for relatively narrow reflections.

[Insert Fig. 7 about here]

4.3 Results of fitting and discussion

By the fitting, simultaneously to all observed diffraction patterns recorded at various values of ψ using the model and the procedure described in section 3, the observed reflection profiles can be reproduced well. Slight discrepancies occur for the peak positions and peak shifts of especially reflections with φ_{hkl} close to 0°, measured at different values of ψ. This may be an artefact due to the adopted isotropy of the elastic constants. Non-ideal ε-Fe_3N_{1+x} (deviating from the ideal composition Fe_3N and/or deviating from the ideally ordered nitrogen distribution) may be more pronouncedly elastically anisotropic than predicted by the applied first-principles calculations for ideal Fe_3N. Further, for the peak profiles of specimen *B* the high-angle tails of high-φ_{hkl} reflections at low ψ could not be described fully adequately. It can be said that the *simultaneous* fitting procedure applied to all measured reflections for different values of ψ, using the partitioned lattice-parameter profiles and the linear stress-depth profile as microstructure model, led to a satisfactory description of the measured data. In the following, the obtained results for the fit parameters are presented and discussed.

4.3.1 Lattice-parameter-depth profiles

Indeed, as expected for nitrogen diffusion-controlled growth of the ε layer, the values of the strain-free lattice parameters *a* and *c* and thus the nitrogen content decrease from the surface to the ε/γ′ interface (Fig. 8). If the nitrogen concentration depends linearly on depth in the ε layers during nitriding [12, 47], application of one-to-one relations between composition and the two hexagonal lattice parameters (e.g. [17, 18]) involves that the lattice parameters $a(z)$ and $c(z)$ should also vary linearly with depth. Since the expected compositions of the ε layers at the surface and at the ε/γ′ interface can be calculated on the basis of nitrogen-absorption isotherms and (local) equilibrium at the ε/γ′ interface [12, 48] (see Table 1), a linear lattice-parameter-depth profile can then be predicted. Such a prediction is not supported by the results obtained here (see Fig. 8). In particular, the depth-dependent lattice parameters obtained by the model fitting do not depend linearly on depth for both specimen *A* and specimen *B*. Moreover, both lattice parameters, *a* and *c*, do not vary in a coupled fashion as it would be expected from the composition dependence of the hexagonal lattice parameters: the relative change of *a* $\left(\delta a^{\text{total}} / a(j=0)\right)$ should be 1.8 times larger than the relative change of *c* (cf. data in Ref. [18]), but experimentally this relative change is 3.4 for specimen *A* and 2.5 for specimen *B*.[6]

[Insert Fig. 8 about here]

The strain-free lattice-parameter data obtained have also been presented in plots of *c* vs. *a* (Fig. 9). In this type of plot the effect of composition is only indirectly revealed by the decrease of both lattice parameters with decreasing nitrogen content. If *a* and *c* would only depend on the nitrogen content prevailing at the depth *z*, all data points should be located on a curve $c = f(a)$. This curve can be calculated by the dependencies of the lattice parameters *a* and *c* on

[6] If one would have imposed in the fitting procedure the one-to-one relations between composition and the lattice parameters from Refs. [17, 18] an unacceptable description of the experimental data would occur.

composition; two examples for (linear) $c = f(a)$ interdependences valid for quenched ε phase have been included in Fig. 9 [17, 18]. Evidently, this does not hold fully for the experimental data: *at the surface* of both specimens *A* and *B* the lattice parameters are compatible with the (for quenched ε phase) predicted interdependences $c = f(a)$ (sample *A*: *a*, *c* of the first grid point; sample *B*: *a*, *c* of the first 5 grid points), whereas systematic deviations from that interdependence occur with increasing depth *z*: for a given value of *a* at a certain depth *z* the value of *c* at the same depth is larger than predicted by the interdependences $c = f(a)$. This anomaly appears to be typical for polycrystalline ε layers, since too large *c*/*a* ratios were not only observed in the present work but were also reported by Liapina et *al*. [22], who analysed (homogenised) ε layers of various nitrogen contents with conventional XRD measurements using $CoK\alpha_1$, thereby obtaining data pertaining to averages for the whole ε layer.

[Insert Fig. 9 about here]

As a possible explanation of the observed deviations from the interdependences $c = f(a)$ as given by [17, 18], it may be suggested that stress in the ε layer (section 4.3.2) may influence the state of nitrogen ordering in the ε phase (and possibly its magnetism), which can influence the lattice parameters [18]. However, the most likely explanation for the too large *c*/*a* ratio close to the ε/γ′ interface is suggested to be the anisotropy of the linear thermal expansion coefficient of ε-Fe_3N_{1+x} [9, 49], which is also likely the origin of the line broadening contribution *f*′ (see section 3.3): The linear coefficient of thermal expansion $\alpha_{\varepsilon,c}$ of the lattice parameter *c*, measured for powders, is much larger (up to about three times, depending on the nitrogen content) than that of the lattice parameter *a*, $\alpha_{\varepsilon,a}$. Such anisotropy leads to strongly direction dependent dimensional changes upon changing temperature. In massive polycrystalline layers, with intrinsically strong grain interaction, the effective lattice-parameter changes due to thermal shrinkage upon cooling

will be less anisotropic than as expected for free standing grains, or possible in powder specimens. Hence, upon cooling the thermal shrinkage in polycrystalline ε layers in *c* directions is less pronounced and in *a* directions more pronounced than strived for; even a close-to-isotropic shrinkage may occur (see also discussion on the macrostress in section 4.3.2). This effect of grain interaction leads to larger values of the lattice parameter *c* and to smaller values of the lattice parameter *a* measured at room temperature, compared to values expected for unconstrained crystallites. Therefore, a too large *c*/*a* lattice-parameter ratio is observed, especially close to the ε/γ′ interface; at the surface grain interaction is less constrained, and therefore the lattice parameters at the surface can be compatible with the concentration dependencies of the lattice parameters corresponding to $c = f(a)$, as observed (see Fig. 9). Similar changes of measured lattice parameters due to anisotropic expansion/shrinkage in combination with grain-interaction effects have been observed for thin layers of NiSi [50].

The lattice parameters at the surface and at the ε/γ′ interface as expected from the nitriding conditions (cf. beginning of section 4.3.1) have been indicated in Fig. 9, too. For both specimens the fitted lattice parameters at the surface as well as at the ε/γ′ interface are larger than the expected values. This might hint at nitrogen contents at the surface and at the ε/γ′ interface larger than expected. To appreciate these differences it is recognised that uncertainties exist for the expected nitrogen contents: for example the phase boundary ε/ε+γ′ (at 823 K) may be located at 24.1 at.% N [12] or at 24.5 at.% N [51], leading to quite large variations in the corresponding lattice parameters.

4.3.2 Residual stress-depth profiles

The residual macrostress-depth profiles within the ε layers of both specimens, as determined by the fitting according to Eq. (2), are similar (Fig. 8). The stress at the surface is tensile, decreases with increasing depth, passing through zero near to the middle of the layers, and becomes compressive close to and at the ε/γ′ interface. The obtained stress value at the surface of specimen

A (about + 90 MPa) is lower than that of specimen *B* (about + 125 MPa); at the ε/γ′ interface the stress amounts for both specimens to about – 95 MPa. Consequently, the total *change* in stress over the whole ε layer is $\delta\sigma_{//}^{\text{total}} = -185$ MPa for specimen *A* and $\delta\sigma_{//}^{\text{total}} = -220$ MPa for specimen *B*, which corresponds to total *changes* in strain of $\delta\varepsilon_{//}^{\text{total}} = -5.3\times10^{-4}$ for specimen *A* and of $\delta\varepsilon_{//}^{\text{total}} = -6.4\times10^{-4}$ for specimen *B*, according to $\delta\varepsilon_{//}^{\text{total}} = \dfrac{\delta\sigma_{//}^{\text{total}}(1-\nu)}{E}$.

The compound layer is attached by cohesion to the ferritic substrate, the latter being much thicker than the compound layer. Thus, the ferrite substrate will be largely stress/strain free, and the linear misfit between the layer and the substrate is accommodated by a (biaxial) state of macrostrain/macrostress in the compound layer. On this basis different sources for the origin of the residual macrostress in the ε layers can be discussed.

(i) Thermal misfit

The observed stress in the ε layer, and in particular the observed total *change* in stress $\delta\sigma_{//}^{\text{total}}$, can be ascribed to thermally induced misfit between the layer and the substrate, as generated by quenching the specimen from the nitriding temperature to ambient temperature (see what follows).

Thermal misfit between the layer and the substrate originates from different coefficients of linear thermal expansion of the ε phase (averaged over the crystallographic orientations, viz. isotropy of thermal expansion is assumed here) and of the α-Fe substrate. Thus, the associated thermal strain in the ε layer parallel to the surface, $\varepsilon_{//}^{\text{th}}$, can be calculated from

$$\varepsilon_{//}^{\text{th}} = \int_{T_1}^{T_2} (\alpha_\varepsilon(z) - \alpha_{\alpha\text{-Fe}})dT \qquad (11)$$

where T_1 and T_2 denote nitriding and ambient temperature, respectively. The average coefficient of linear thermal expansion α_ε of ε-Fe_3N_{1+x} was found to increase with increasing nitrogen content [49, 52] (The increase of (average) α_ε with the nitrogen content (see Fig. 10) appears to be an

acceptable trend as it is also exhibited by ε-phase analogous manganese nitrides [52]). Hence, the presence of a stress gradient in the ε layer can be understood, with the stress becoming (more) compressive for increasing depth below the surface.

[Insert Fig. 10 about here]

A quantitative calculation of the *change* of the thermal misfit strain over the ε layer, $\delta\varepsilon_{//}^{\mathrm{th,total}}$, is possible using

$$\delta\varepsilon_{//}^{\mathrm{th,total}} = \varepsilon_{//}^{\mathrm{th}}\left(z=0\right) - \varepsilon_{//}^{\mathrm{th}}\left(z=Z\right) = \left[\alpha_{\varepsilon}\left(z=0\right) - \alpha_{\varepsilon}\left(z=Z\right)\right]\left[T_2 - T_1\right] \qquad (12)$$

yielding[7] $\delta\varepsilon_{//}^{\mathrm{th,\,total}} = -1.3\times10^{-3}$ for specimen *A* and $\delta\varepsilon_{//}^{\mathrm{th,total}} = -1.7\times10^{-3}$ for specimen *B*, corresponding to total *changes* in stress over the ε layer, given by $\delta\sigma_{//}^{\mathrm{th,total}} = \dfrac{\delta\varepsilon_{//}^{\mathrm{th,total}}\times E}{\left(1-\nu\right)}$, of $\delta\sigma_{//}^{\mathrm{th,total}} = -460$ MPa for specimen *A* and of $\delta\sigma_{//}^{\mathrm{th,total}} = -580$ MPa for specimen *B*. The larger value of $\delta\varepsilon_{//}^{\mathrm{th,total}} / \delta\sigma_{//}^{\mathrm{th,total}}$ for specimen *B*, as compared to specimen *A*, is consistent with the larger compositional variation present in specimen *B* corresponding with a larger change in α_{ε}. However, the calculated stress changes are about 2.5 times larger than the measured stress changes. Moreover, the prediction on the basis of the data for the linear thermal expansion coefficient in Fig. 10 involves that at the surface still a compressive stress should prevail. This can be discussed as follows.

Already small inaccuracies of the adopted values for the thermal expansion coefficients can explain the discrepancy: For example, see the various values for $\alpha_{\alpha\text{-Fe}}$ compiled in literature [19, 21, 53] vary, and, in particular, the values of α_{ε} are likely of limited accuracy, because these

[7] The isotropic coefficient of thermal expansion α_{ε} was assumed to vary linearly with concentration and the values used for α_{ε} at the surface and at the ε/γ′-interface were obtained by inter- and extrapolation, respectively, at nitrogen content values pertaining to the surface and the ε/γ′ interface (see Table 1).

values were determined from temperature-dependent lattice-parameter data ranging from ambient temperature to at maximum 713 K, whereas the nitriding temperature in this work was 823 K. The use of an isotropic average of the (intrinsically anisotropic; see section 4.3.1) coefficient of linear thermal expansion of the ε phase may also induce errors. Since the macrostrain/macrostress present in the ε phase at a certain depth is determined by the *difference* of the thermal expansion coefficients of the ε layer and the α-Fe substrate (see Eq. (11)), small inaccuracies of both adopted expansion coefficients will already significantly affect the calculated depth-dependent values of the strain/stress. Further, differences between the observed and calculated strain values may also be due to macrostrain relaxation within the first 50 K to 100 K during cooling [1].

The difference between the observed stress/strain and the predicted thermally induced stress/strain discussed above may be (partially) due to the presence of additional contributions discussed under points (ii)-(iv).

(ii) Compositionally induced strain

It can be assumed that the specific volume (i.e. volume per Fe atom) increase upon transformation of γ′ into ε at the ε/γ′ is accommodated plastically (see (iii) below). Then, during compound-layer growth elastic accommodation of the specific volume increase within the ε layer due to the increase of the nitrogen content from the ε/γ′ interface to the surface will lead to a (with respect to the thermal stress) additional depth-dependent stress contribution. This contribution counteracts the thermally induced stress-depth profile, as can be understood as follows: At the ε/γ′ interface the volume of the unstrained ε unit cell is smaller than at the surface. Hence, for the same amount of iron atoms per unit area parallel to the surface, a compressive stress parallel to the surface develops that becomes larger with decreasing distance to the surface. The largest value of compositionally induced strain, $\varepsilon_{//}^{c}$, occurs at the surface and equals

$$\varepsilon_{//}^{c} = (V_{\varepsilon/\gamma'\text{-interface}} - V_{\text{surface}}) / V_{\text{surface}} \times \tfrac{1}{3} \qquad (13)$$

where $V_{\varepsilon/\gamma'\text{-interface}}$ and V_{surface} are the volumes of the ε unit cell at the ε/γ′ interface and at the surface, respectively. Using values for the lattice parameters at the surface and at the ε/γ′ interface as obtained by the fitting procedure, the compositionally induced strain at the surface amounts for specimen *A* to $\varepsilon_{//}^{c} = -3.0\times10^{-3}$ and for specimen *B* to $\varepsilon_{//}^{c} = -4.3\times10^{-3}$. These strain values are relatively large and it may be expected that the compositional misfit within the ε layer is accommodated to a significant extent plastically (cf. [1, 21]). In any case this possible source of residual stress cannot explain the occurrence of tensile stress at the surface.

(iii) Volume misfit

During growth of the compound layer volume misfits due to the different specific volumes per solvent (= iron) atom of α-Fe, γ′-Fe_4N_{1-y} and ε-Fe_3N_{1+x} occur at the γ′/α and ε/γ′ interfaces: The specific volume of γ′ at the γ′/α interface is about 15.0 % larger than that of α-Fe and the specific volume of ε at the ε/γ′ interface is about 16.7 % larger than that of α-Fe (i.e. 1.4 % larger than the specific volume of γ′ at the ε/γ′ interface). Taking the very thick, with respect to the compound layer, α-Fe substrate as completely rigid, and if these misfits would be accommodated fully elastically, compressive stresses in both sublayers, γ′ and ε, would be induced during growth of these phases. However, the results by Somers and Mittemeijer, 1990 [1] indicate that for γ′ this volume misfit is accommodated fully plastically and this misfit does not contribute to the residual stress as observed after nitriding at ambient temperature. Recognising fully plastic accommodation of the volume misfit at the γ′/α interface, a possible elastic accommodation of the ε/γ′ interfacial volume misfit would lead to a strain of $\varepsilon_{//}^{\text{vol}} = -4.7\times10^{-3}$ in the ε layer. This value is much larger than the value found at the ε/γ′ interface. Therefore it may be assumed that the volume misfit strain occurring upon the γ′ to ε transformation is also accommodated plastically and thus does not contribute to the observed stress at the ε/γ′ interface.

(iv) Strain relaxation due to pore formation

Porosity in the surface-adjacent region of the ε layer can lead to the reduction of stress as compared to a massive layer. The formation of porosity in iron nitrides is very common [54, 55] and can be attributed to the metastable nature of the iron nitrides with respect to the decomposition into iron and molecular nitrogen gas at normal pressure [12, 45, 55]. Pores form mainly upon longer treatment times and for higher nitrogen contents. Thus it can be understood that pore formation had occurred only very *slightly* in the near-surface region of specimen *B* and not for specimen *A* (cf. Fig. 1). Hence, the effect of strain relaxation due to porosity can be neglected for the presently studied specimens.

Somers and Mittemeijer, 1992 [21] discussed, mainly theoretically, stress-depth profiles within ε-Fe_3N_{1-x} layers on the basis of several different contributions. In that work also a stress gradient was found experimentally (by XRD measurements) by successive sublayer removals, which is generally in agreement with the present study: the stress was found to be zero at the surface and becoming compressive with increasing distance to the surface. The presence of the stress gradient was explained, contrary to the present interpretation, to be caused by (in that case distinct) porosity at the surface (stress relaxation) and due to elastic accommodation of the volume misfit between ε and γ′ during growth. The effect of the thermal misfit could not be estimated since no precise data for thermal expansion of ε were known (it was assumed $\alpha_{\gamma'} < \alpha_{\varepsilon} < \alpha_{\alpha\text{-Fe}}$). In other works [19, 20] tensile stresses were found in the near-surface region of ε-$Fe_3(N,C)_{1+x}$ layers, which is compatible with the present results. However, the analysed compound layers were grown on steel substrates and partially also generated by nitrocarburising processes and then consequently carbon was taken up in the compound layers, further complicating the problem and therefore no straightforward interpretation was possible.

5 *Conclusions*

A consistent interpretation of both the diffraction-line shift and the anisotropic diffraction-line broadening, with respect to both the crystal frame of reference and the specimen frame of reference, is possible for hexagonal ε-Fe_3N_{1+x} layers using a model for the microstructure comprising the simultaneous presence of composition- and stress-depth profiles. Depth-dependent strain-free lattice parameters and stress values can be determined by fitting of the model to the full profiles of several reflections *hkl* recorded at different specimen-tilt angles.

Application of this model to high-resolution X-ray powder diffraction patterns recorded at various specimen-tilt angles, using synchrotron radiation, from two different polycrystalline ε-Fe_3N_{1+x} layers grown on α-Fe by gas nitriding at 823 K revealed that:

(i) The macrostrain-free lattice-parameter-depth profiles in the ε layers are caused by the depth dependence of the nitrogen contents within the layers with high nitrogen contents at the surface and low nitrogen contents at the ε/γ′ interface. The observed line broadening is mainly due to this compositional variation, which corresponds to the different nitriding conditions of the two analysed specimens. The values of the strain-free lattice parameters *a* and *c* decrease from the surface to the ε/γ′ interface. Away from the surface of the ε layer, grain interaction counteracting the crystallographically anisotropic thermal shrinkage of the ε phase leads to too large *c*/*a* lattice-parameter ratios as observed at room temperature.

(ii) The macrostress-depth profiles in the ε layers are induced by cooling the ε layer after nitriding to room temperature. The concentration dependence of the average coefficient of thermal expansion of ε-Fe_3N_{1+x} leads to tensile stress at the surface and to compressive stress at the ε/γ′ interface, since the coefficient of thermal expansion of ε-Fe_3N_{1+x} is larger than that of α-Fe for high nitrogen content and smaller than that of α-Fe for low nitrogen content.

The X-ray diffraction method proposed and applied in this paper allows the non-destructive simultaneous determination of composition- and stress-depth profiles by combining line-profile analysis and diffraction-stress analysis: in one step several *hkl* diffraction-line profiles

(each) recorded at various angles of specimen tilt are fitted simultaneously. Thereby the method developed is applicable to a wide range of other specimens, as solid state diffusion couples.

Acknowledgement

The authors are greatful to Mr. Jürgen Köhler for his help with the nitriding experiments and to Dr. Ewald Bischoff for performing the EBSD measurements. We also wish to thank Mr. Peter Kobold and Dr. Peter van Aken for TEM analysis. Special thanks go to Dr. Shunli Shang (Pennsylvania State University, Pennsylvania, USA) for calculating the elastic constants of ε-Fe_3N and to Dr. Michael Knapp (CELLS, Barcelona, Spain), who assisted during the measurements at the beamline B2, DESY, Hasylab (Hamburg, Germany).

Appendix

First-principles calculations of the elastic constants of ε-Fe_3N

First-principles calculations of the five independent elastic constants (at 0 K) for hexagonal ε-Fe_3N were performed employing the *Vienna ab initio simulation package* VASP [56, 57] in a similar fashion as described for γ′-Fe_4N [32]. The obtained elastic stiffness constants C_{ij} of ε-Fe_3N are $C_{11} = 313.72$ GPa, $C_{12} = 141.82$ GPa, $C_{13} = 131.50$ GPa, $C_{33} = 329.17$ GPa and $C_{44} = 105.65$ GPa. The small differences between C_{11} and C_{33}, C_{12} and C_{13} as well as of $(C_{11} - C_{12})/2$ and C_{44} indicate a relatively small elastic anisotropy. Therefore, isotropically averaged elastic constants were calculated out of the anisotropic constants, leading to: $C_{11} = C_{33} = 321.46$ GPa, $C_{12} = C_{13} = 133.65$ GPa, $C_{44} = (C_{11} - C_{12})/2 = 93.90$ GPa. Thus it can be calculated (cf. [34]): Young's modulus $E = 243$ GPa and Poisson's ratio $v = 0.29$. These last, isotropic values were used in this work.

References

[1] M.A.J. Somers and E.J. Mittemeijer, Metall. Trans. A **21A** 189 (1990).

[2] D. Liedtke, U. Baudis, J. Boßlet, *et al.* Wärmebehandlung von Eisenwerkstoffen. Renningen: Expert Verlag, 2006.

[3] C.H. Knerr, T.C. Rose and J.H. Filkowski. ASM Handbook Heat Treating: ASM International, 1991.

[4] T. Bell, Heat Treat. Met. **2** 39 (1975).

[5] C. Dawes and D.F. Tranter, Heat Treat. Met. **3** 70 (1985).

[6] K.H. Jack, Proc. R. Soc. London, A **195** 34 (1948).

[7] K.H. Jack, Acta Crystallogr **5** 404 (1952).

[8] A. Leineweber, H. Jacobs, F. Hüning, *et al.*, J. Alloys Compd. **288** 79 (1999).

[9] A. Leineweber, H. Jacobs, F. Hüning, *et al.*, J. Alloys Compd. **316** 21 (2001).

[10] B.J. Kooi, M.A.J. Somers and E.J. Mittemeijer, Metall. Mater. Trans. A **27A** 1055 (1996).

[11] H.A. Wriedt, N.A. Gokcen and R.H. Nafziger, Bull Alloy Phase Diagr **8** 355 (1987).

[12] E.J. Mittemeijer and M.A.J. Somers, Surf. Eng. **13** 483 (1997).

[13] A. Burdese, Metall. Ital. **49** 195 (1957).

[14] R.J. Bouchard, C.G. Frederick and V. Johnson, J. Appl. Phys. **45** 4067 (1974).

[15] D. Firrao, B. De Benedetti and M. Rosso, Metall. Ital. **9** 373 (1979).

[16] W.-D. Jentzsch and S. Böhmer, Krist. Tech. **12** 1275 (1977).

[17] M.A.J. Somers, B.J. Kooi, L. Maldzinski, *et al.*, Acta Mater. **45** 2013 (1997).

[18] T. Liapina, A. Leineweber, E.J. Mittemeijer, *et al.*, Acta Mater. **52** 173 (2004).

[19] H. Oettel and B. Ehrentraut, Härterei-Tech. Mitt. **40** 183 (1985).

[20] H.C.F. Rozendaal, P.F. Colijn and E.J. Mittemeijer, Surf. Eng. **1** 30 (1985).

[21] M.A.J. Somers and E.J. Mittemeijer, Härterei-Tech. Mitt. **47** 175 (1992).

[22] T. Liapina, A. Leineweber and E.J. Mittemeijer, Metall. Mater. Trans. A **37A** 319 (2006).

[23] T. Liapina, A. Leineweber and E.J. Mittemeijer, Scripta Materialia **48** 1643 (2003).

[24] R. Chatterjee-Fischer, R. Bodenhagen, F.-W. Eysell, *et al.* Wärmebehandlung von Eisen und Stahl - Nitrieren und Nitrocarburieren. Renningen-Malmsheim: Expert Verlag, 1995.

[25] P.F. Colijn, E.J. Mittemeijer and H.C.F. Rozendaal, Z. Metallkd. **74** 620 (1983).

[26] A. Wells, J. Mater. Sci. **20** 2439 (1985).

[27] A. Strecker, U. Salzberger and J. Mayer, Prakt. Metallogr. **30** 482 (1993).

[28] C. Middendorf and W. Mader, Z. Anorg. Allg. Chem. **627** 398 (2001).

[29] M. Knapp, C. Baehtz, H. Ehrenberg, *et al.*, J. Synchr. Rad. **11** 328 (2004).

[30] U. Welzel, J. Ligot, P. Lamparter, *et al.*, J. Appl. Crystallogr. **38** 1 (2005).

[31] R. Delhez, T.H. de Keijser and E.J. Mittemeijer, Surf. Eng. **3** 331 (1987).

[32] T. Gressmann, M. Wohlschlögel, S. Shang, *et al*., Acta Mater **55** 5833 (2007).

[33] P.D. Evenschor, W. Fröhlich and V. Hauk, Z. Metallkunde **62** 38 (1971).

[34] C.J. Howard and E.H. Kisi, J. Appl. Crystallogr. **32** 624 (1999).

[35] NIST. X-ray attenuation tables: http://physics.nist.gov/PhysRefData/FFast/html/form.html. 2006.

[36] T. Liapina, A. Leineweber, E.J. Mittemeijer, *et al.*, Z. Kristallogr. Suppl. **23** 449 (2006).

[37] A.A. Coelho, J. Appl. Crystallogr. **33** 899 (2000).

[38] T.G. Berger, A. Leineweber, E.J. Mittemeijer, *et al.*, Z. Kristallogr. Suppl. **23** 443 (2006).

[39] A.A. Coelho. TOPAS: General Profile and Structure Analysis Software for Powder Diffraction Data. Karlsruhe, Germany: Bruker AXS GmbH, 2003.

[40] R. Louboutin and D. Louër, Acta Cryst. A **25** 335 (1969).

[41] D. Gerardin, J.P. Morniroli, H. Michel, *et al.*, J. Mater. Sci. **16** 159 (1981).

[42] T. Schubert, H. Oettel and D. Bergner, Härterei-Tech. Mitt. **41** 370 (1986).

[43] X. Xu, L. Wang, Z. Yu, *et al.*, Metall. Mater. Trans. A **27A** 1347 (1996).

[44] Z.Q. Liu, Z.K. Hei and D.X. Li, J. Mater. Res. **17** 2621 (2002).

[45] C. Middendorf and W. Mader, Z. Metallkunde **94** 333 (2003).

[46] A. Leineweber and E.J. Mittemeijer, J. Appl. Crystallogr. **37** 123 (2004).

[47] M.A.J. Somers and E.J. Mittemeijer, Metall. Mater. Trans. A **26A** 57 (1995).

[48] L. Maldzinski, Z. Przylecki and J. Kunze, Steel Research **57** 645 (1986).

[49] A. Leineweber. Ordnungsverhalten von Stickstoff sowie Magnetismus in binären Nitriden einiger 3d-Metalle: Mn/N, Fe/N und Ni/N. Göttingen: Cuvillier Verlag, 1999.

[50] C. Detavernier, C. Lavoie and F.M. d'Heurle, J. Appl. Phys. **93** 2510 (2003).

[51] B.J. Kooi, M.A.J. Somers and E.J. Mittemeijer, Metall. Mater. Trans. A **27A** 1063 (1996).

[52] A. Leineweber, H. Jacobs, W. Kockelmann*, et al.*, J. Alloys Compd. **384** 1 (2004).

[53] Y.S. Touloukian, R.K. Kirby, R.E. Taylor*, et al.* Thermal Expansion: Metallic Elements and Alloys. New York: IFI/Plenum, 1977.

[54] M.A.J. Somers and E.J. Mittemeijer, Surf. Eng. **3** 123 (1987).

[55] B. Prenosil, Härterei-Tech. Mitt. **28** 157 (1973).

[56] G. Kresse and J. Furthmüller, Comp. Mat. Sci. **6** 15 (1996).

[57] G. Kresse and J. Furthmüller, Phys. Rev. B: Condens. Matter **54** 11169 (1996).

[58] E.J. Mittemeijer and J.T. Slycke, Surf. Eng. **12** 152 (1996).

Table 1: Parameters pertaining to the nitriding at 823 K of specimens *A* and *B*. The nitriding potential*, $r_N = p_{NH_3} / p_{H_2}^{3/2}$, the measured ε-layer and γ′-layer thicknesses and the according to the nitriding conditions expected nitrogen contents in the ε phase at the surface [48] and at the ε/γ′ interface [12].

specimen	treatment time [h]	NH_3 content [vol.%]	H_2 content [vol.%]	nitriding potential r_N [$atm^{-1/2}$]	ε-layer thickness [µm]	γ′-layer thickness [µm]	maximum N content at the surface [at.% N]	minimum N content at the ε/γ′ interface [at.% N]
A	1.5	56	44	1.92	3.0	1.8	25.7	24.1
B	5.0	60	40	2.37	9.4	1.3	26.2	24.1

* The nitriding potential r_N is commonly used to quantify the chemical potential of nitrogen in NH_3/H_2 (at 1 atm) gas mixtures, which is considerable higher than that of molecular N_2 at 1 atm [58].

Fig. 1.

Optical micrographs (bright field) of compound-layer cross sections (after Nital etching) of the analysed gas nitrided α-iron specimens, consisting of an outer ε-Fe_3N_{1+x} layer and an inner γ′-Fe_4N layer: (a) specimen *A* (1.5 h, 823 K, 56/44 vol.% NH_3/H_2), (b) specimen *B* (5.0 h, 823 K, 60/40 vol.% NH_3/H_2)

Fig. 2.

Part of the metastable Fe-N phase diagram [11]. Note the break at the abscissa. The filled points connected by the dashed line indicate the nitrogen contents of ε compound layers at the surface (approximately; in equilibrium with the gas phase) and at the ε/γ′ interface, as expected for nitriding at 823 K. The concentration-depth profile in the ε layer is due to the inward diffusion of nitrogen during the nitriding process. The nitrogen content of the annealed (at 673 K), homogenised reference sample, used for the line-broadening contribution *f*′, has been indicated by the open circle.

Fig. 3.

Schematic illustration of the partitioning of the ε-Fe_3N_{1+x} compound layer (total thickness *Z*) into *n* sublayers of equal thickness $\delta z = Z/n$. The strain-free lattice spacings $d_{hkl,0}$ at the grid points GP ($j = 0, 1, \ldots, n$) decrease with increasing distance to the surface due to the corresponding decrease of nitrogen content. *Within* the sublayers ($j = 1, 2 \ldots, n$) the lattice spacings are taken to depend linearly on depth. Variation of the tilt angle ψ leads to variation of the observed lattice spacing (see dashed line for $d_{hkl,\psi}$) as due to the presence of an (assumedly linear) stress-depth profile.

Fig. 4.

Theoretically expected constitution of the diffraction-line profile of reflection *hkl* at a tilt angle ψ originating from the partitioning of the ε layer (neglecting here for simplicity the effect of X-ray absorption, which additionally occurs): all sublayers give rise to the same integrated intensity. Assuming that each slice of lattice spacing $d_{hkl,\psi}$ diffracts independently and since each sublayer has its own lattice-spacing variation, different subprofile breadths and heights on the diffraction-angle scale 2θ occur.

Fig. 5.

Cross-sectional EBSD image of the compound layer of specimen *A*, showing a columnar grain structure of the ε layer with grain boundaries more or less perpendicular to the surface. The different grey shades represent different crystal-grain orientations.

Fig. 6.

Cross-sectional high-resolution TEM image at the ε/γ′ interface region of specimen *A*. The insets are Fourier transforms taken from the ε and γ′ parts of the image, corresponding to diffraction patterns, for ε and γ′. These Fourier transforms indicate a $[1\,\bar{1}0]$ zone-axis orientation of the ε phase. The γ′ phase is not oriented along a low-index zone axis (in the image only (111) planes are visible). Evidently, the orientation relationship mentioned in Refs. [28, 41-45] is not observed.

Fig. 7.

Section of the X-ray high-resolution diffraction patterns of (a) specimen *A* and (b) specimen *B* recorded at different tilt angles ψ. The intensities of the reflections were scaled for better visibility (the original data were considered in the fitting process). The full lines through the measured data

points represent the fitted curves obtained on basis of the applied model (the γ′-111 reflection which occurs additionally for specimen *A*, at strongly ψ dependent 2θ positions, was fitted separately using a pseudo-Voigt function). The bottom lines represent the difference curves for $\psi = 0°$ (top), $\psi = 30°$ (middle) and $\psi = 60°$ (bottom). The lines were shifted vertically in order to separate them.

Fig. 8.

Strain-free lattice-parameter and stress-depth profiles of the ε layer of (a) specimen *A* and of (b) specimen *B* as determined by fitting on the basis of all recorded diffraction patterns. The values of both lattice parameters, *a* and *c*, decrease with increasing distance to the surface. The total changes of δa and δc are larger for specimen *B* than for specimen *A*, which is compatible with the applied nitriding conditions (Table 1). The stress is for both specimens of tensile nature at the surface, decreases with increasing depth and becomes of compressive nature near the ε/γ′ interface.

Fig. 9.

Lattice parameter *c* vs. lattice parameter *a* of (a) specimen *A* and (b) specimen *B*. At the surface the lattice parameters are in good agreement with interdependences $c = f(a)$ proposed by Refs. [17] and [18] for quenched ε phase. Approaching the ε/γ′ interface the *c*/*a* ratio increases with respect to these relations. The open stars indicate the expected lattice parameters at the surface (ε in equilibrium with the gas phase at 823 K) and the filled stars indicate the expected lattice parameters at the ε/γ′ interface (ε in equilibrium with γ′ at 823 K).

Fig. 10.

The concentration dependence of the coefficient of thermal expansion of the ε phase (isotropic average), α_ε [52], including a fitted straight line. With increasing nitrogen content α_ε increases: at low nitrogen contents α_ε is smaller than $\alpha_{\alpha\text{-Fe}}$, whereas at higher nitrogen contents α_ε is larger than $\alpha_{\alpha\text{-Fe}}$.The value for $\alpha_{\alpha\text{-Fe}} = 1.47\times10^{-6}\ K^{-1}$ was obtained by integration over the temperature interval from 293 K to 823 K [53] and holds only for pure iron.

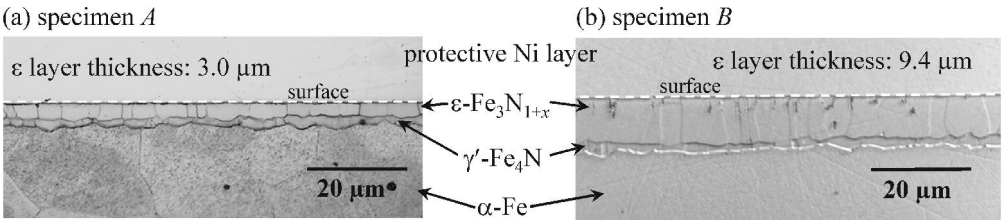

Figure 1
164x34mm (600 x 600 DPI)

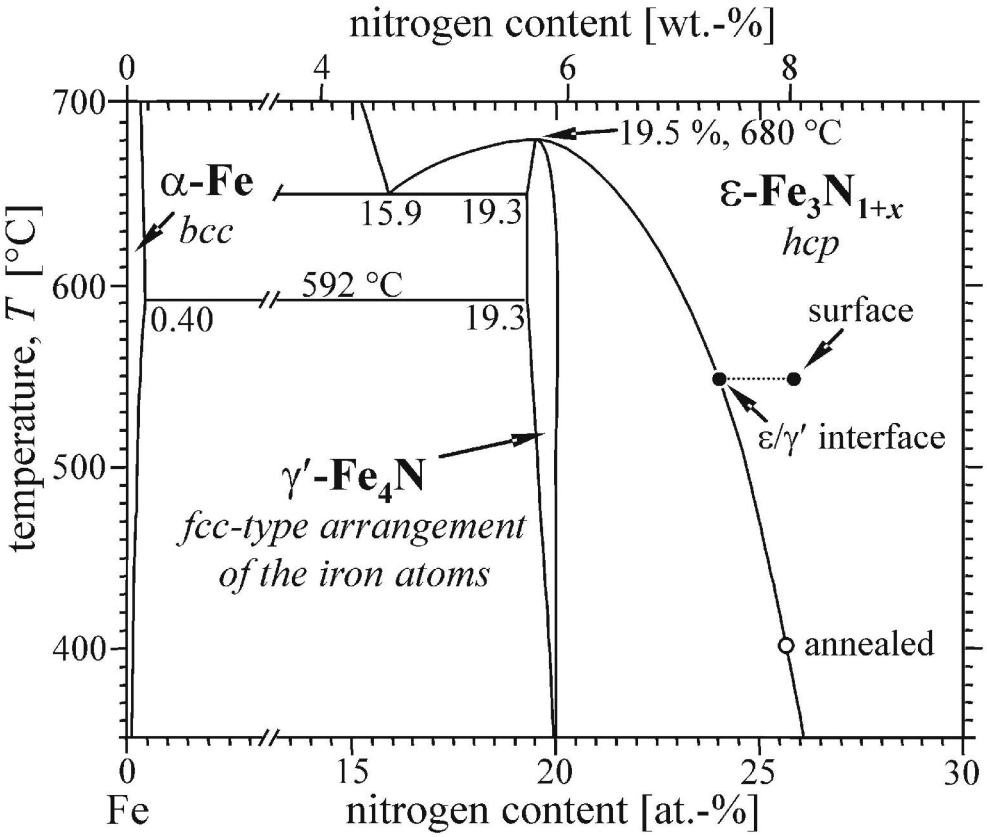

Figure 2
105x89mm (600 x 600 DPI)

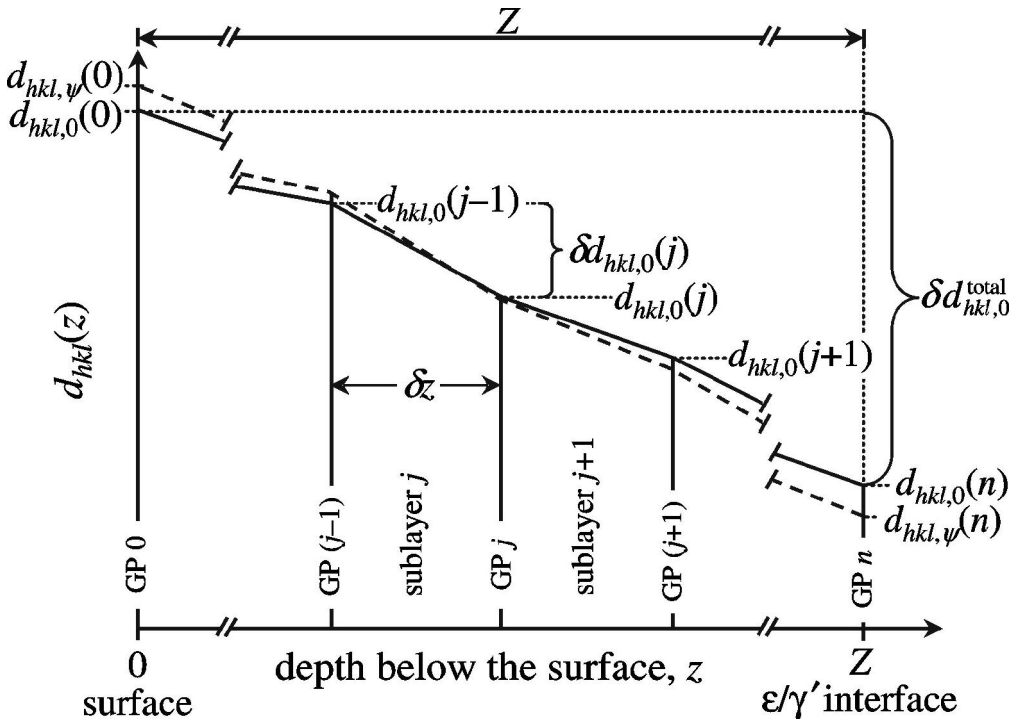

Figure 3
67x47mm (600 x 600 DPI)

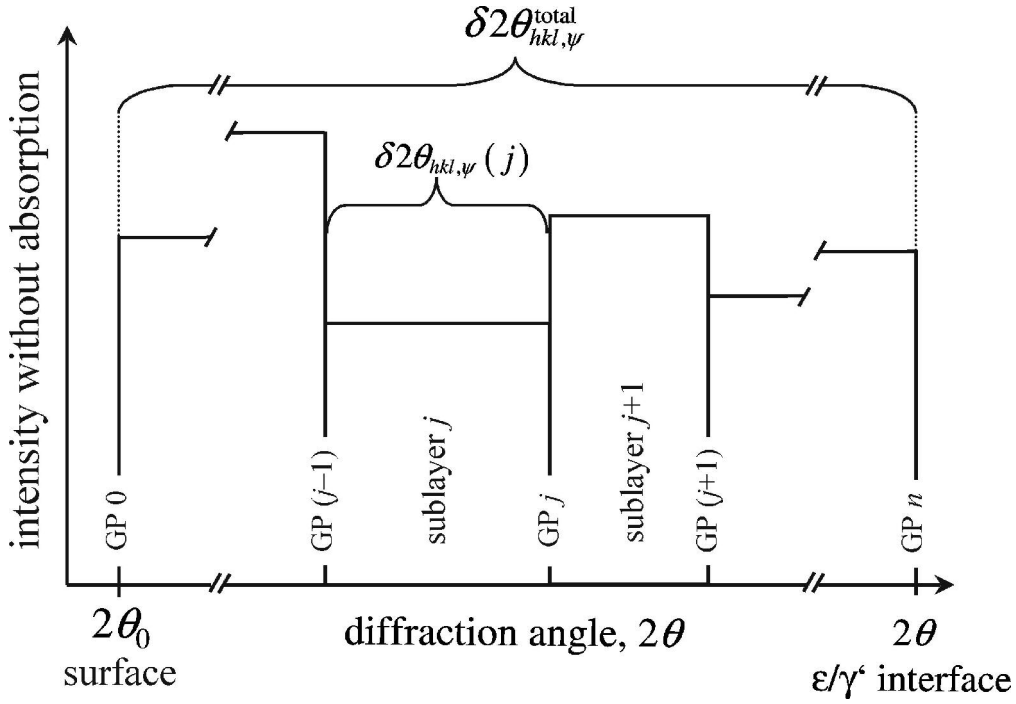

Figure 4
107x74mm (600 x 600 DPI)

Figure 5
100x19mm (600 x 600 DPI)

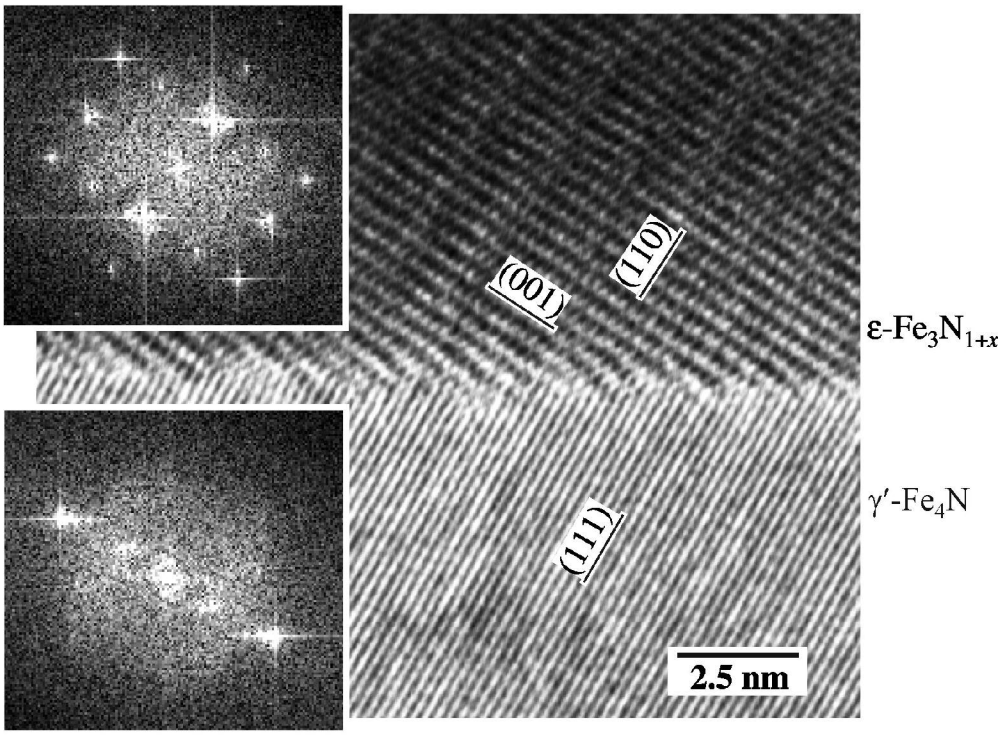

Figure 6
74x54mm (600 x 600 DPI)

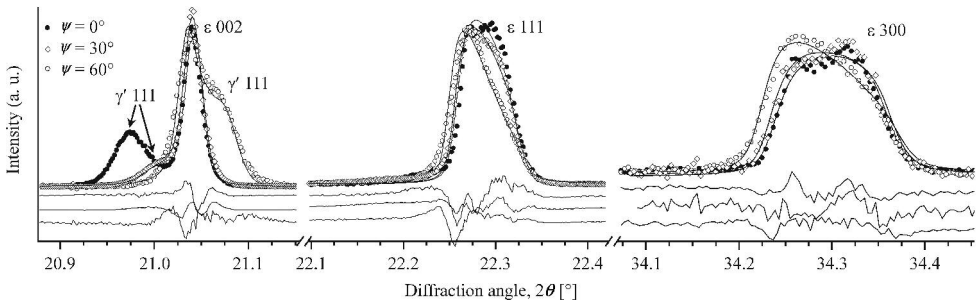

Figure 7a
237x73mm (600 x 600 DPI)

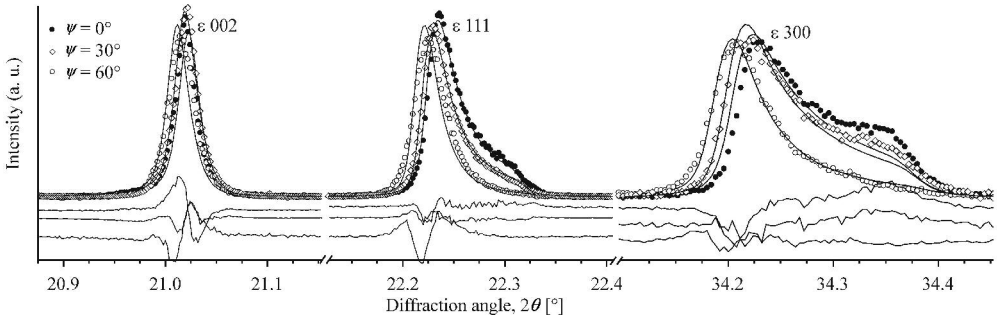

Figure 7b
230x71mm (600 x 600 DPI)

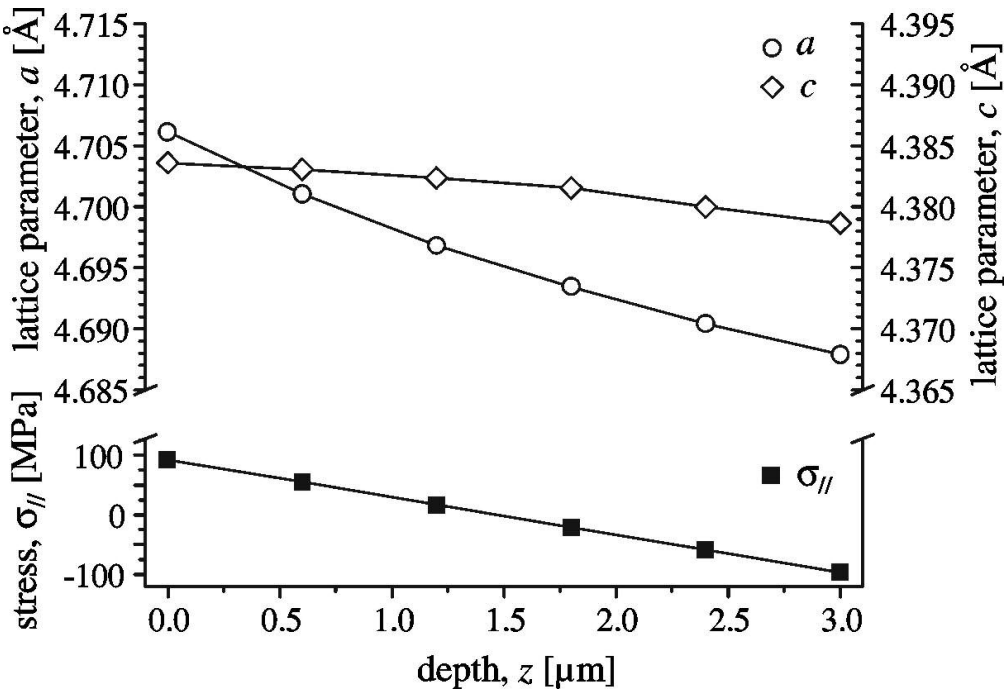

Figure 8a
51x34mm (600 x 600 DPI)

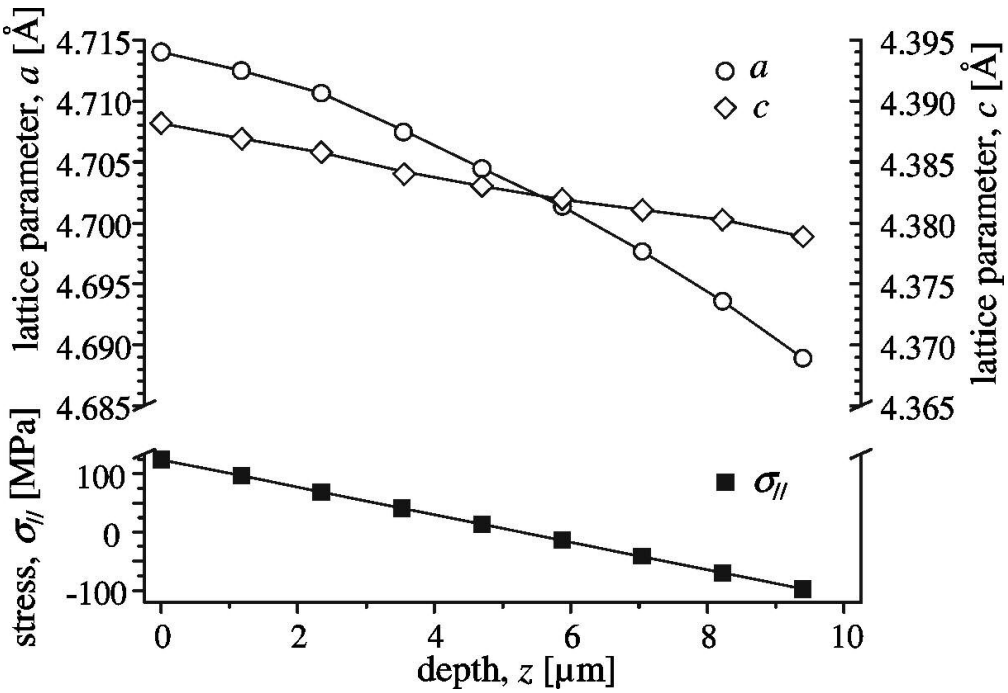

Figure 8b
51x34mm (600 x 600 DPI)

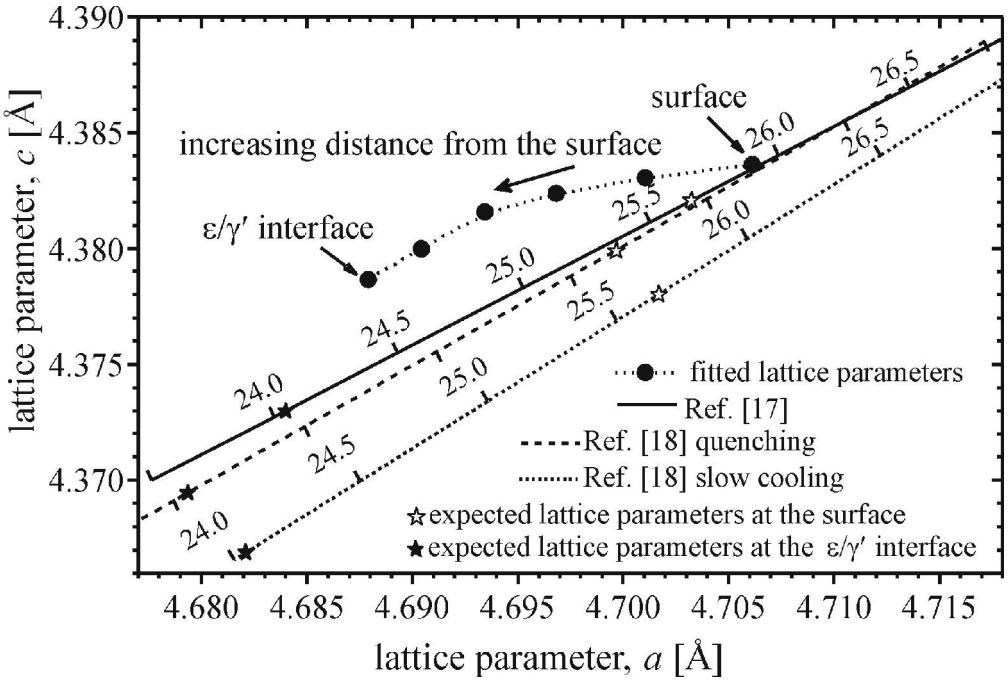

Figure 9a
84x56mm (600 x 600 DPI)

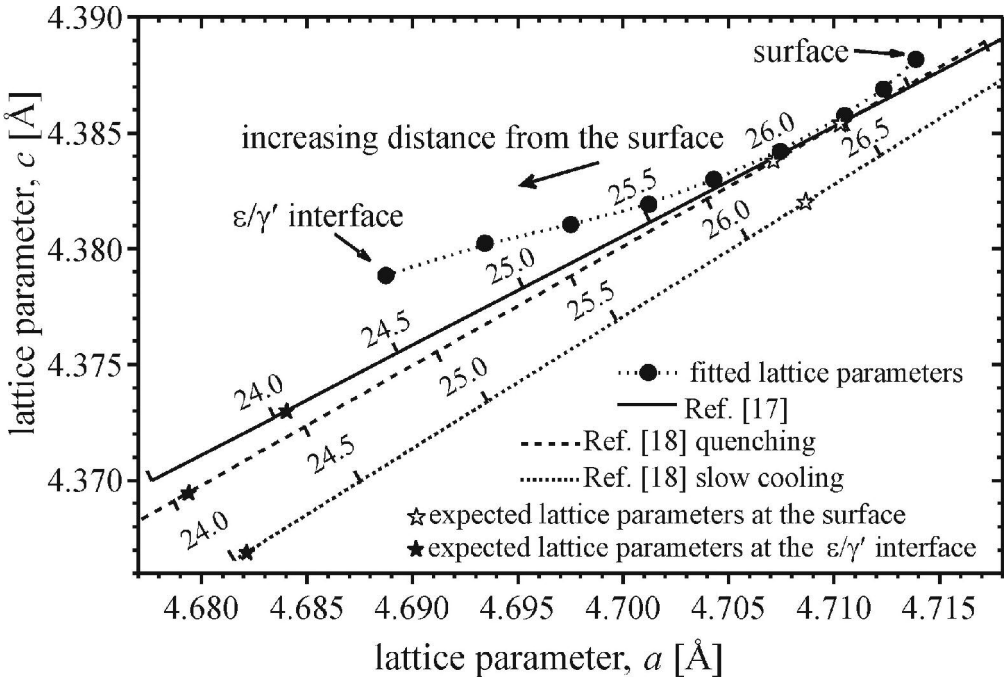

Figure 9b
84x56mm (600 x 600 DPI)

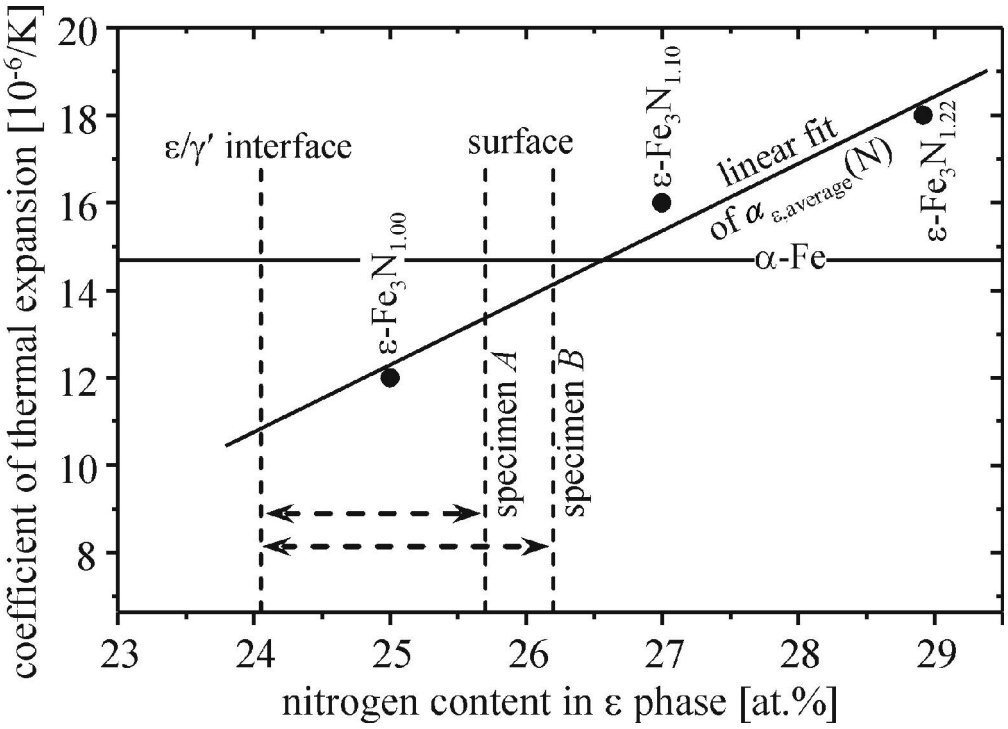

Figure 10
76x55mm (600 x 600 DPI)